Theor Chem Acc (2012) 131:1237
DOI 10.1007/s00214-012-1237-4

REGULAR ARTICLE

Spectrum simulation and decomposition with nuclear ensemble: formal derivation and application to benzene, furan and 2-phenylfuran

Rachel Crespo-Otero · Mario Barbatti

Received: 12 February 2012 / Accepted: 14 May 2012 / Published online: 9 June 2012

Abstract A formal derivation of the nuclear-ensemble method for absorption and emission spectrum simulations is presented. It includes discussions of the main approximations employed in the method and derivations of new features aiming at further developments. Additionally, a method for spectrum decomposition is proposed and implemented. The method is designed to provide absolute contributions of different classes of states (localized, diffuse, charge-transfer, delocalized) to each spectral band. The methods for spectrum simulation and decomposition are applied to the investigation of UV absorption of benzene, furan, and 2-phenylfuran, and of fluorescence of 2-phenylfuran.

Keywords Electronic spectrum · Absorption · Fluorescence · Spectrum simulation · Excimer · 2-Phenylfuran

Dedicated to Professor Marco Antonio Chaer Nascimento and published as part of the special collection of articles celebrating his 65th birthday.

Electronic supplementary material The online version of this article (doi:10.1007/s00214-012-1237-4) contains supplementary material, which is available to authorized users.

R. Crespo-Otero (✉) · M. Barbatti (✉)
Max-Planck-Institut für Kohlenforschung,
Kaiser-Wilhelm-Platz 1, 45470 Mülheim an der Ruhr, Germany
e-mail: crespo@kofo.mpg.de

M. Barbatti
e-mail: barbatti@kofo.mpg.de

1 Introduction

Visible and ultraviolet spectroscopy is a central technique for general material characterization. Its fundamental role is still enhanced when dealing with photo-active molecules employed in photo-receptors, light emitters and photovoltaics. From the theoretical standpoint, the characterization of the electronic spectrum of molecules is often restricted to characterization of vertical transitions and their energies and transition dipole moments. This procedure greatly aids the assignment of measured spectra, but is far from representing its complexity. Full spectrum simulation, beyond simple vertical-lines computation, is a much more involved task, demanding non-routine and computationally costly procedures, such as propagation of excited-state nuclear wave packets or determination of Franck–Condon factors [1, 2]. In general, such simulations are strongly limited in terms of nuclear degrees of freedom or number of electronic states considered. They are also non-black-box procedures, which require high degree of specialization to be conducted, precluding them of being adopted as routine procedures for researchers out of the computational-chemistry field.

Recently, there have been efforts to develop general methods for spectrum simulation more accessible to the quantum-chemical community and aiming at large molecules. Examples of such developments are the implementation of the Tannor–Heller method [3, 4] in the ORCA program, which allows computing vibrational progressions, and of the quadratic-coupling expansion in Gaussian, which allows computing vibrational progressions and dark vibronic bands [5]. Moreover, spectrum simulations based on excitation of an ensemble of nuclear geometries have become popular [6–8]. This kind of approach is based on the hypothesis that the spectral band shape is determined

by the ground-state nuclear-geometry distribution. When this hypothesis is approximately fulfilled, the nuclear-ensemble approach can provide good estimates for several spectral features, including vibrational broadening of short lived states, dark vibronic bands, and absolute spectral intensities. Additionally, the nuclear-ensemble approach includes all degrees of freedom and can be extended to large number of excited states. The conceptual simplicity and relative low computational cost makes the nuclear-ensemble approach ideal for routine simulations. The nuclear-ensemble approach, however, has a number of handicaps, namely (1) it depends on arbitrary parameters; (2) it cannot properly predict vibrational broadening of long-lived states; (3) it cannot predict vibrational progressions; and (4) it does not properly take into account vibronic features of the energy gap of the spectral lines.

The origin of each element composing the nuclear-ensemble approach can be traced back to decades ago, first with the works of Heller, Wilson and others in the 1980s, where absorption bands were computed based on molecular dynamics [9]. It is also influenced by the works of Skinner [10], which provided a useful link between Kubo's stochastic theory of the line shape [11] and molecular dynamics, and by the reflection principle [12], which approaches bound to continuum transitions from the nuclear-ensemble perspective. The intuitive character of the nuclear-ensemble approach has created a situation where although the method is frequently employed, there is no clear derivation of its formalism. This information gap makes difficult to understand the reasons for its limitations and to propose ways to improve the method. In this contribution, we derive equations for absorption cross sections and radiative decay rates based on the nuclear-ensemble method. The main approximations are made explicit, and improvements on the method are proposed, in particular ways to get rid of arbitrary parameters.

One of the advantages of the nuclear-ensemble approach is that it provides straightforward ways to analyze different contributions summing up to the full spectrum. For instance, in Ref. [7], the UV absorption spectra of nucleobases have been decomposed in terms of their several diabatic contributions. In Ref. [13], the absorption spectrum of $Cr(CO)_6$ has been decomposed in terms of symmetry contributions. In Ref. [14], the spectrum of urocanic acid has been decomposed in terms of isomeric contributions. In all these cases, the spectral decomposition helped to reveal the character of states forming the several bands. In the present work, we develop a new way to perform spectral decomposition analysis, now, based on the electronic-density distribution of the states. This approach allows characterizing the contributions of localized states, charge-transfer states, diffuse states and excimer states to each band.

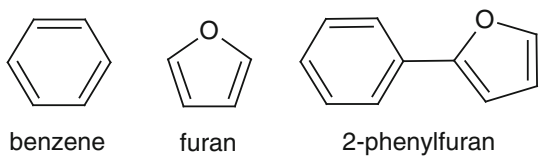

Fig. 1 Illustration of benzene, furan and 2-phenylfuran

Another advantage of the nuclear-ensemble approach is that it is naturally a post-Condon approximation. Because the transition moments are evaluated for geometries displaced from equilibrium position, vibronic contributions to the spectrum are computed without need of Herzberg–Teller type of expansions [5]. Thus, even dark vibronic bands are described by the simulations [15].

Often in the literature, computed vertical excitations are compared to experimental band maxima. Although this is a valid procedure to provide assignments and to check the overall quality of theoretical method, it can also be misleading, when one does not take into account that the band maximum is normally red-shifted in relation to the vertical excitation. The spectrum simulation allows computing the shift between these two quantities. This shift is used to estimate the experimental value of the vertical excitation, which is a more appropriate quantity to have the theoretical data compared with.

To illustrate several of these methodological features, we have investigated the absorption and emission spectra of 2-phenylfuran and of its constituent monomers, benzene and furan (Fig. 1). A series of features lead us to this particular choice of molecules for our benchmark investigations. First, a good deal of experimental and theoretical data is available for all three molecules. Second, all three molecules are small enough to have their spectra simulated with even more accurate (and costly) methods than the nuclear-ensemble approach, allowing methodological comparisons. Third, there is an interesting physical chemistry associated with these molecules: While benzene and furan are non-fluorescent species, 2-phenylfuran is fluorescent [16].

2 Derivation of the nuclear-ensemble method

2.1 Absorption cross section

With the formalism of the time-dependent perturbation theory for interaction between an electron and the classical radiation field, within the electric dipole and Born–Oppenheimer approximations, the isotropic absorption cross section is given by [17]

$$\sigma(E) = \frac{\pi}{3\hbar c\varepsilon_0 n_r E}\sum_{n,k}\int \left|\Delta E_{00,nk}(\mathbf{R})\chi^*_{00}(\mathbf{R})\langle\phi_0|\mu(\mathbf{r},\mathbf{R})\right. \\ \left.|\phi_n\rangle_{\mathbf{r}}\chi_{nk}(\mathbf{R})\right|^2\delta\left(\Delta E_{00,nk}(\mathbf{R}) - E\right)\mathrm{d}\mathbf{R}, \quad (1)$$

where E is the photon energy of the probe radiation, ε_0 is the vacuum permittivity, c is the speed of light, n_r is the refractive index of the medium, and μ is the dipole operator. The sum runs over the final electronic states n and vibrational states k. The molecule is supposed to be initially in the electronic and vibrational ground state. The electronic and nuclear wavefunctions are represented by ϕ and χ, respectively. The δ function selects the resonant frequency between the initial and the final states. The ket indexes indicate the integration coordinates, $\mathbf{r}$ for electronic and $\mathbf{R}$ for nuclear. The resonance occurs for

$$\Delta E_{00,nk} = E_{nk} - E_{00} + \Delta E_{0,n}, \quad (2)$$

where $\Delta E_{0,n}$ is the vertical excitation energy and E_{00} and E_{nk} are the vibrational energies of the ground and excited states.

The cross section can be recast in the time domain as [3]

$$\sigma(E) = \frac{1}{6\hbar^2 c\varepsilon_0 n_r E}\sum_n \mathrm{Re}\int \Delta E^2_{0,n}(\mathbf{R})M^2_{0n}(\mathbf{R}) \\ \times\left[\int \chi^*_{00}(\mathbf{R})\chi_n(\mathbf{R},t)\mathrm{e}^{i(E+E_{00})t/\hbar}\mathrm{d}t\right]\mathrm{d}\mathbf{R}, \quad (3)$$

where M_{0n} is the electronic transition dipole moment given by

$$M_{0n}(\mathbf{R}) = \langle\phi_0|\mu_e(\mathbf{r};\mathbf{R})|\phi_n\rangle_{\mathbf{r}} \quad (4)$$

and where the following approximation was employed

$$\Delta E_{0,n} \approx \left\langle\Delta E_{00,nk}\right\rangle_k. \quad (5)$$

The term between brackets in Eq. (3) is the inverse Fourier transform of the overlap between the ground-state nuclear wavefunction and the wave packet $|\chi_n(t)\rangle$ given by the operation of the excited-state Hamiltonian H_n on the ground-state wavefunction:

$$|\chi_n(t)\rangle = \mathrm{e}^{-iH_n t/\hbar}|\chi_{00}\rangle. \quad (6)$$

The extinction coefficient ε for photoabsorption (in L mol^{-1} cm^{-1}) can be written in terms of the absorption cross section σ (in cm^2) as

$$\varepsilon = \frac{10^{-3}N_\mathrm{A}}{\ln(10)}\sigma, \quad (7)$$

where N_A is the Avogadro constant.

The core of the method is to compute the overlap functions

$$\varphi(\mathbf{R},t) = \chi^*_{00}(\mathbf{R})\chi_n(\mathbf{R},t), \quad (8)$$

which are needed to integrate Eq. (3). In the Tannor–Heller approach [3], for instance, the computation of the overlap function is done within the Condon approximation employing harmonic oscillator wavefunctions. For the nuclear-ensemble approaches explored in the present work, which goes beyond the Condon approximation, we proceed without explicit computation of overlap functions. In the next sections, two phenomenological models for the overlap function are discussed. These models, however, depend on arbitrary parameters. In Sect. 2.3, we discuss how to get rid of these parameters. Although the results discussed here are restricted to these two models, the derivation itself is rather general and can be adapted to other choices of overlap functions, including explicitly computed overlap functions obtained from wave packet propagation.

2.2 Overlap function: approximation 1

To get the result discussed in Ref. [7], the overlap function is approximated by

$$\chi^*_{00}(\mathbf{R})\chi_n(\mathbf{R},t) \\ = |\chi_{00}(\mathbf{R})|^2\exp\left[-\frac{\delta_n}{2\hbar}|t| - \frac{i}{\hbar}\Delta E_{0,n}(\mathbf{R})t - \frac{i}{\hbar}E_{00}(\mathbf{R})t\right], \quad (9)$$

where δ_n is a parameter associated with the lifetime of state n. Inserting Eq. (9) in Eq. (3) and performing the integration over t result in

$$\sigma(E) = \frac{\pi\hbar e^2}{2mc\varepsilon_0 n_r E}\sum_n\int |\chi_{00}(\mathbf{R})|^2\Delta E_{0,n}(\mathbf{R})f_{0n}(\mathbf{R}) \\ \times g_\mathrm{Lorentz}\left(E - \Delta E_{0,n}(\mathbf{R}),\delta_n\right)\mathrm{d}\mathbf{R}. \quad (10)$$

where e and m are the electron charge and mass. For convenience, the transition dipole moment has been expressed in terms of oscillator strengths [18]:

$$M^2_{0n} = \frac{3\hbar^2 e^2}{2m\Delta E_{0,n}}f_{0n}. \quad (11)$$

In Eq. (10), g_Lorentz is a normalized Lorentzian line shape given by

$$g_\mathrm{Lorentz}\left(E - \Delta E_{0,n},\delta_n\right) = \frac{1}{\pi}\frac{\delta_n/2}{\left(E - \Delta E_{0,n}(\mathbf{R})\right)^2 + (\delta_n/2)^2}. \quad (12)$$

2.3 Overlap function: approximation 2

In the harmonic approximation, neglecting Duschinksky effects and frequency shifts between the ground and excited states, the nuclear wavefunction overlap (integrated over $\mathbf{R}$) can be written as [3]

$$\langle \chi_{00} \mid \chi_n(t) \rangle = \exp\left[\sum_j \left(\frac{-\Delta_{nj}^2}{2}\left(1 - \mathrm{e}^{-i\omega_j t}\right) - \frac{i\omega_j t}{2} \right) + \frac{i}{\hbar}\Delta E_{0,n}^a t \right], \quad (13)$$

where sum runs over all normal modes j with frequency ω_j. Δ_{nj} (dimensionless) is the component along normal mode j of the displacement vector between the ground- and excited-state equilibrium positions. $\Delta E_{0,n}^a$ is the energy difference between the minima of the excited state n and of the ground state. By expanding the exponential term in the exponential argument in a power series of t, we see that the first non-imaginary term in the equation above is proportional to t^2. The equation including all terms until the second order becomes

$$\langle \chi_{00} \mid \chi_n(t) \rangle \approx \exp\left[-i\left(\frac{1}{2}\sum_j \left(\Delta_{nj}^2 + 1 \right)\omega_j + \omega_{0n}^a \right) t - \frac{1}{2}\left(\sum_j \Delta_{nj}^2 \omega_j^2 \right) t^2 \right]. \quad (14)$$

Since the non-imaginary terms are actually those responsible for the line width, Eq. (14) motivates a new functional form for the overlap function:

$$\chi_{00}^* \chi_n(\mathbf{R}, t) = |\chi_{00}(\mathbf{R})|^2 \exp\left[-\frac{i}{\hbar}\Delta E_{0,n}(\mathbf{R}) t - \frac{i}{\hbar}\varepsilon_n t - \frac{i}{\hbar}E_{00} t - \frac{1}{8\hbar^2}\delta_n^2 t^2 \right]. \quad (15)$$

As we shall see, Eq. (14) is obtained from Eq. (15) under the condition that $\Delta E_{0,n}(\mathbf{R})$ is approximately constant over $\mathbf{R}$.

Inserting Eq. (15) in Eq. (3) and integrating over t leads to

$$\sigma(E) = \frac{\pi\hbar e^2}{2mc\varepsilon_0 n_r E} \sum_n \int |\chi_{00}(\mathbf{R})|^2 \Delta E_{0,n}(\mathbf{R}) f_{0n}(\mathbf{R}) \times g_{\mathrm{Gauss}}\left(E - \Delta E_{0,n}(\mathbf{R}) - \varepsilon_n(\mathbf{R}), \delta_n\right) \mathrm{d}\mathbf{R}, \quad (16)$$

which, different from the previous result, Eq. (10), has normalized Gaussian line shapes

$$g_{\mathrm{Gauss}}\left(E - \Delta E_{0,n}(\mathbf{R}) + \varepsilon_n(\mathbf{R}), \delta_n\right) = \frac{1}{\left(2\pi(\delta_n/2)^2\right)^{1/2}} \exp\left(\frac{-\left(E - \Delta E_{0,n}(\mathbf{R}) - \varepsilon_n\right)^2}{2(\delta_n/2)^2} \right) \quad (17)$$

instead of Lorentzian line shapes and includes vibronic shifts through the ε_n term.

Another difference regarding the comparison between Eqs. (10) and (16) is that this second approximation for the overlap function gives us a direct way to determine the parameters δ_n and ε_n. Although we will not investigate state-specific line widths and vibronic shifts in the simulations discussed in this work, for completeness of the derivation, it is worth showing how these parameters can be computed. If $\Delta E_{0,n}(\mathbf{R})$ is approximately constant over $\mathbf{R}$, then δ_n and ε_n in Eq. (15) can be obtained by comparison with Eq. (14) and be defined in terms of and of ω_j, Δ_{nj}, and $\delta E_{0,n} = \Delta E_{0,n} - \Delta E_{0,n}^a$ as:

$$\varepsilon_n = \frac{\hbar}{2}\sum_j \Delta_{nj}^2 \omega_j - \delta E_{0,n}, \quad (18)$$

$$\delta_n = 2\hbar\left(\sum_j \Delta_{nj}^2 \omega_j^2 \right)^{1/2}. \quad (19)$$

Still in the harmonic approximation without Duschinsky rotation or frequency shifts, these quantities are simply (see details in the Online Resource 1)

$$\varepsilon_n = -\frac{1}{2}\sum_j \frac{G_{nj}^2}{\mu_j \omega_j^2} = -\frac{1}{2}\delta E_{0,n}, \quad (20)$$

$$\delta_n = 2\left(\hbar \sum_j \frac{G_{nj}^2}{\mu_j \omega_j} \right)^{1/2}, \quad (21)$$

where

$$G_{nj} = \left. \frac{\mathrm{d}E_n}{\mathrm{d}q_j} \right|_{q_j = 0} \quad (22)$$

is the excited-state potential energy gradient evaluated at the ground-state minimum geometry with respect to the ground-state normal coordinates $\mathbf{q}$.

2.4 Nuclear-ensemble approximation

The integrals on $\mathbf{R}$ in Eqs. (10) and (16) can be computed employing a Monte Carlo procedure sampling N_p random $\mathbf{R}_l$values according to the distribution $|\chi_{00}(\mathbf{R}_l)|^2$ [19]:

$$\sigma(E) = \frac{\pi e^2 \hbar}{2mc\varepsilon_0 n_r E} \sum_n^{N_{fs}} \frac{1}{N_p} \sum_l^{N_p} \Delta E_{0,n}(\mathbf{R}_l) f_{0n}(\mathbf{R}_l) \times g(E - \Delta E(\mathbf{R}_l), \delta_n). \quad (23)$$

In this equation, g is a normalized Lorentzian line shape centered at $\Delta E = \Delta E_{0,n}$ for the integration of Eq. (10) and a normalized Gaussian line shape centered at $\Delta E = \Delta E_{0,n} + \varepsilon_n$ for integration of Eq. (16). Note that the sum over the states was restricted to a number N_{fs} of final states.

A convenient way of sampling the ground-state density at time zero is to suppose that the harmonic approximation is valid and to employ a Wigner distribution

$$|\chi_{00}(\mathbf{q})|^2 = \prod_{j=1}^{3N-6} \left(\frac{\mu_j \omega_j}{\pi\hbar}\right)^{1/2} \exp\left(-\mu_j \omega_j q_j^2/\hbar\right). \quad (24)$$

Using a stochastic algorithm, an ensemble of N_p normal coordinates $\{\mathbf{q}_l\}$ ($l = 1 - N_p$) can be generated according to the Wigner distribution and converted into an ensemble of Cartesian geometries $\{\mathbf{R}_l\}$. Alternatively, a ground-state ensemble $\{\mathbf{R}_l\}$ can also be generated by trajectories simulations in the ground state. In this case, however, one should care that the kinetic energy in the internal vibrational degrees is high enough as to provide the zero-point energy for each degree of freedom. As discussed in Ref. [20], when the vibrational temperature is properly taken into account, Wigner and trajectory samplings tend to produce equivalent results. Either way, after having an ensemble of geometries distributed according to $|\chi_{00}(\mathbf{R})|^2$, and $\Delta E_{0,n}$ and f_{0n} computed for each geometry in the ensemble, $\sigma(E)$ can be evaluated using Eq. (23).

The error in the cross section due to the statistical sampling can be estimated by

$$\delta\sigma(E) \simeq \frac{\pi e^2 \hbar}{2mc\varepsilon_0 n_r E} \sum_{n}^{N_{fs}} \frac{1}{N_p^{1/2}\left(N_p - 1\right)^{1/2}} \times \left[\sum_{l}^{N_p} \left(\Delta E_{0n}(\mathbf{R}_l) f_{0n}(\mathbf{R}_l) g\left(E - \Delta E_{0,n}(\mathbf{R}_l), \delta_n\right) - \langle s_n \rangle\right)^2\right]^{1/2}, \quad (25)$$

where

$$\langle s_n \rangle = \frac{1}{N_p} \sum_{l'}^{N_p} \Delta E_{0n}(\mathbf{R}_{l'}) f_{0n}(\mathbf{R}_{l'}) g\left(E - \Delta E_{0,n}(\mathbf{R}_{l'}), \delta_n\right). \quad (26)$$

2.5 Emission spectrum

The differential rate for radiative emission (dimensionless) is given by [2, 21]

$$\Gamma_{\mathrm{rad}}(E) = \frac{n_r^3}{3\pi\hbar^3 c^3 \varepsilon_0} \times \sum_{k,m} \rho_k^T \int \Delta E_{1k,0m}(\mathbf{R})^3 \left|\chi_{0m}^*(\mathbf{R}) \times \langle \phi_0 | \mu(\mathbf{r}, \mathbf{R}) | \phi_1 \rangle_{\mathbf{r}} \chi_{1k}(\mathbf{R})\right|^2 \delta\left(E - \Delta E_{1k,0m}(\mathbf{R})\right) \mathrm{d}\mathbf{R}, \quad (27)$$

where the emission is supposed to occur from the kth vibrational state of the first-excited electronic state, into the mth vibrational state of the ground electronic state. At a certain temperature T, state k is populated according to the Boltzmann distribution

$$\rho_k^T = \frac{\mathrm{e}^{-(E_{1k} - E_{10})/k_{\mathrm{B}}T}}{\sum_{k'} \mathrm{e}^{-(E_{1k'} - E_{10})/k_{\mathrm{B}}T}}. \quad (28)$$

Following Ref. [21], we have adopted an empirical n_r^3 dependence of the differential emission rate on the refractive index. Since the final emission rate should also take into account the dependence on the absorption intensity, which depends itself on n_r^{-1}, the final emission rate should bear an n_r^2 dependence, as experimentally observed [22].

In the time domain, the differential emission rate becomes

$$\Gamma_{\mathrm{rad}}(E) = \frac{n_r^3}{6\pi^2\hbar^3 c^3 \varepsilon_0} \mathrm{Re} \int \Delta E_{1,0}(\mathbf{R})^3 M_{01}^2(\mathbf{R}) \times \left[\sum_k \rho_k^T \int \chi_{1k}^*(\mathbf{R}) \chi_0(\mathbf{R}, t) \mathrm{e}^{i(E_{1k} - E)t/\hbar} \mathrm{d}t\right] \mathrm{d}\mathbf{R}, \quad (29)$$

where the following approximation was employed

$$\Delta E_{1,0} \approx \left\langle \Delta E_{1k,0m} \right\rangle_{k,m}. \quad (30)$$

Now, the wave packet is given by operating the ground-state Hamiltonian H_0 on the excited-state wavefunction:

$$|\chi_0(t)\rangle = \mathrm{e}^{-iH_0 t/\hbar} |\chi_{1k}\rangle. \quad (31)$$

With an overlap-function approximation similar to the first approximation discussed above for absorption,

$$\chi_{1k}^*(\mathbf{R}) \chi_0(\mathbf{R}, t) = |\chi_{1k}(\mathbf{R}_l)|^2 \times \exp\left[-\alpha_n(\mathbf{R})|t| + i\omega_{01}(\mathbf{R})t - i\omega_{1k}(\mathbf{R})t\right], \quad (32)$$

we obtain

$$\Gamma_{\mathrm{rad}}(E) = \frac{e^2 n_r^3}{2\pi\hbar m c^3 \varepsilon_0} \int \left[\sum_k \rho_k^T |\chi_{1k}(\mathbf{R})|^2\right] \times \Delta E_{1,0}(\mathbf{R})^2 |f_{10}(\mathbf{R})| g_{\mathrm{Lorentz}}\left(E - \Delta E_{1,0}(\mathbf{R}), \delta\right) \mathrm{d}\mathbf{R}. \quad (33)$$

This last expression can be integrated with a Monte Carlo procedure:

$$\Gamma_{\mathrm{rad}}(E) = \frac{e^2 n_r^3}{2\pi\hbar m c^3 \varepsilon_0} \frac{1}{N_p} \sum_{l}^{N_p} \Delta E_{1,0}(\mathbf{R}_l)^2 |f_{10}(\mathbf{R}_l)| \times g_{\mathrm{Lorentz}}\left(E - \Delta E_{1,0}(\mathbf{R}_l), \delta\right), \quad (34)$$

where N_p random $\mathbf{R}_l$ points are sampled according to the $\sum_k \rho_k^T |\chi_{1k}(\mathbf{R}_l)|^2$ distribution. Within the harmonic approximation, the density of the nuclear ensemble is

simply given by the Wigner distribution for a specific temperature T [23]:

$$\sum_k \rho_k^T |\chi_{1k}(\mathbf{q})|^2 = \left|\chi_{10}^T(\mathbf{q})\right|^2 = \prod_{j=1}^{3N-6} \left(\frac{\mu_j^1 \omega_j^1}{2\pi\hbar \sinh\left(\hbar\omega_j^1 / k_B T\right)} \right)^{1/2} \times \exp\left(-\frac{\mu_j^1 \omega_j^1}{\hbar} q_j^2 \tanh\left(\frac{\hbar\omega_j^1}{2k_B T}\right) \right), \quad (35)$$

where μ_j^1 and ω_j^1 refer to reduced masses and angular frequencies of the electronic excited state.

The quantity Γ_{rad} expresses the rate of spontaneous emission per molecule per unit of angular frequency between $E/\hbar$ and $(E + dE)/\hbar$ [2]. For a single fluorescence band, in the absence of non-radiative processes, the radiative decay rate (κ_{rad}) and the maximum lifetime (τ_0) are given by

$$\kappa_{rad} = 1/\tau_0 = \frac{1}{\hbar} \int \Gamma_{rad}(E) dE. \quad (36)$$

2.6 Comments on the line shapes

Usually, the discussion on the line shape of the broadening of spectroscopic lines is made in terms of homogeneous and inhomogeneous broadening [2, 10]. Lorentzian line shapes are associated with homogeneous broadening caused by the natural lifetime of the lines, while Gaussian line shapes are associated with inhomogeneous broadening caused by thermodynamics events like collisions. In the derivation of the nuclear-ensemble method, we have seen that the Lorentzian and Gaussian line shapes were directly connected to the time dependence of the vibrational overlap function. While the exponential decay (Eq. 9) resulted in a Lorentzian line shape, a Gaussian decay (Eq. 15) resulted in a Gaussian line shape.

We can also relate these two approximations through the stochastic theory of the line shape developed by Kubo [11] and applied to molecular line shapes by Saven and Skinner [10]. As shown by Kubo, the overlap function given by Eq. (13) is a general result for a Gaussian-distributed random variable in a Markovian process [11]. In the limit of a very slow decay of the time-correlation function of this random variable, the overlap function reduces to Eq. (9) and the line has a Lorentzian shape. In the limit of a very fast decay of the time-correlation function, the overlap function reduces to Eq. (15) and the line has a Gaussian shape. Employing molecular dynamics simulations of chromophores within non-polar fluids, Saven and Skinner [10] showed that Kubo's model works well in these two limits, but cannot produce accurate line shapes in intermediary regimes. They also found out that inhomogeneous broadening (Gaussian lines) dominates the line shapes, unless the spectra are measured at very low temperature.

Although in practical terms, the difference between spectra computed with Eq. (23) employing Lorentzian or Gaussian line shapes is minimal, Gaussian line shapes lend a more physical interpretation to the simulations. When the molecule absorbs a photon, the excited wave packet should accelerate out of the Franck–Condon region [24]. Thus, the overlap function should change slowly initially, as expressed by a Gaussian overlap function. Moreover, as we have seen, the line width is proportional to the energy gradient at the Franck–Condon region (Eq. 21). When the gradient is small, the excited wave packet remains in the Franck–Condon region for a long time, resulting in a narrow spectral line, like those often observed for Rydberg states. When the energy gradient is large, the wave packet moves quickly out of the Franck–Condon region, creating broad bands, like those typically observed in $\pi\pi^*$ excitations.

In the case of molecules holding conical intersections between excited states, the wave packet will quickly populate different states due to the non-adiabatic transitions [25]. Part of this effect is captured by the nuclear-ensemble approach because it populates different states according to their diabatic features (which are determined by the transition dipole moments). But the contribution of the non-adiabatic phenomenon itself for the population of different states is not accounted at all with the overlap functions proposed in the previous sections.

3 Spectrum decomposition

In a system composed of various molecular units, it is of general interest to know how, for a specific electronic state, the electronic density is distributed among the units. Here, we will considerer systems composed of two molecular units, but the generalization for a larger number of units is straightforward. The aim is to implement an automatic analysis algorithm, which can be applied for every electronic state, for each point in the nuclear ensemble, and that returns the state classification in terms of pre-established classes. These classes are (1) local excitation within unit A; (2) local excitation within unit B; (3) delocalized excitation (excimer) involving A and B; (4) diffuse excitation (Rydberg) involving A and B; (5) charge transfer from A to B; and (6) charge transfer from B to A.

We start by expressing the excited-state electronic wavefunction Ψ_I for state I as a singly excited configuration interaction wavefunction (CIS)

$$\Psi_I = \sum_{i\to j} C^I_{i\to j}\Phi_{i\to j}, \tag{37}$$

where $\Phi_{i\to j}$ is a Slater determinant for single excitation from molecular orbital ψ_i into molecular orbital ψ_j. In the case of electronic states computed with TD-DFT approach, the CI coefficients $C^I_{i\to j}$ are given by the time-dependent amplitudes, while the molecular orbitals are given by Kohn–Sham orbitals.

If the ground state can be represented by a restricted closed shell determinant, the density difference between state I and the ground state is given by (after integrating over the electron coordinates)

$$\begin{aligned}\Delta P_{I0} \equiv P_I - P_0 &= \sum_{i\to j}\left(C^I_{i\to j}\right)^2\sum_{\mu\nu}\left(c_{\mu j}c_{\nu j} - c_{\mu i}c_{\nu i}\right)S_{\mu\nu}\\ &\equiv \sum_{i\to j}\left(C^I_{i\to j}\right)^2\left(\rho^j - \rho^i\right),\end{aligned} \tag{38}$$

where $S_{\mu\nu} \equiv \langle\phi_\mu|\phi_\nu\rangle$ is the overlap integral elements between basis functions ϕ_μ, and ϕ_ν and $c_{\mu a}$ are the molecular-orbital coefficients for orbital a and basis function. (Detailed derivation of Eq. (38) is given in the Online Resource 1.)

If the molecular system is split in two units A and B, ΔP_{I0} can be partitioned between basis functions centered in atoms belonging to unit A and atoms belonging to unit B:

$$\begin{aligned}\Delta P_{I0} &= \sum_{i\to j}\left(C^I_{i\to j}\right)^2\left[\sum_{\mu\in A,\nu\in A}\left(c_{\mu j}c_{\nu j} - c_{\mu i}c_{\nu i}\right)S_{\mu\nu}\right.\\ &\quad + \sum_{\mu\in B,\nu\in B}\left(c_{\mu j}c_{\nu j} - c_{\mu i}c_{\nu i}\right)S_{\mu\nu}\\ &\quad \left. + 2\sum_{\mu\in A,\nu\in B}\left(c_{\mu j}c_{\nu j} - c_{\mu i}c_{\nu i}\right)S_{\mu\nu}\right]\\ &\equiv \sum_{i\to j}\left(C^I_{i\to j}\right)^2\left[\left(\rho^j_{AA} - \rho^i_{AA}\right) + \left(\rho^j_{BB} - \rho^i_{BB}\right)\right.\\ &\quad \left. + 2\left(\rho^j_{AB} - \rho^i_{AB}\right)\right].\end{aligned} \tag{39}$$

The distribution of the ρ^k_{AB} electronic density between the molecular units can be done employing standard schemes for the calculation of atomic charges [26]. Here, we employ the simplest approach, the Mulliken partition, where ρ^k_{AB} is distributed equally between A and B. In spite of the well-known handicaps of this partition scheme, it serves well our purposes of qualitatively assigning a large number of electronic states. Employing the Mulliken partition, Eq. (39) is recast as

$$\begin{aligned}\Delta P_{I0} &= \sum_{i\to j}\left(C^I_{i\to j}\right)^2\left[\left(\rho^j_{AA} + \rho^j_{AB} - \rho^i_{AA} - \rho^i_{AB}\right)\right.\\ &\quad \left. + \left(\rho^j_{BB} + \rho^j_{AB} - \rho^i_{BB} - \rho^i_{AB}\right)\right]\\ &= \sum_{i\to j}\left(C^I_{i\to j}\right)^2\left[\left(\rho^j_A - \rho^i_A\right) + \left(\rho^j_B - \rho^i_B\right)\right],\end{aligned} \tag{40}$$

where

$$\begin{aligned}\rho^k_A &\equiv \rho^k_{AA} + \rho^k_{AB},\\ \rho^k_B &\equiv \rho^k_{BB} + \rho^k_{AB}\end{aligned} \tag{41}$$

with $k = i, j$.

In the case of Rydberg orbitals, this partition of the electronic density may not work well because of their very diffuse character. Therefore, the first step in the classification of the electronic states is to detect transitions into Rydberg orbitals. In some particular cases, the detection of these orbitals can be simply done by monitoring the quantity $2\rho^j_{AB}/(\rho^j_{AA} + \rho^j_{BB})$. (See Online Resource 1 for a discussion on this point.) After detecting the Rydberg orbitals, their contribution to each state I is computed by $cR = \sum_m (C^I_m)^2$, with m running over all transition where j is a Rydberg orbital. If cR is equal or larger than a certain threshold t_R, then state I is classified as a diffuse (Rydberg) state.

If $cR < t_R$, the charge transfer is calculated. Because $\Delta P_{I0} = 0$, all change of density in unit A in Eq. (40) must correspond to a complementary change in unit B. Therefore, to obtain the amount of charge transfer between the two units, it is enough to compute the quantity:

$$\mathrm{TCT}^I_A = \sum_{i\to j}\left(C^I_{i\to j}\right)^2\left(\rho^j_A - \rho^i_A\right), \tag{42}$$

where transitions into Rydberg states are excluded from the summation. If $\mathrm{TCT}^I_A > t_{\mathrm{CT}}$, state I is classified as a charge transfer from B to A. If $\mathrm{TCT}^I_A < -t_{\mathrm{CT}}$, the state is classified as charge transfer from A to B. In both cases, t_{CT} is a positive threshold value.

If $\left|\mathrm{TCT}^I_A\right| \le t_{\mathrm{CT}}$, the electronic state can still be either a localized state or a delocalized state (excimer). To distinguish between them, a third threshold value t_L is used. For each transition within state I, if $\rho^i_A/\rho^i_B \ge t_L$, then the transition belongs to the sub-set m_A. If $\rho^i_B/\rho^i_A \ge t_L$, then the transition belongs to a sub-set m_B. The total localization of state I within units A and B is evaluated as $cA = \sum_{m_A}\left(C^I_{m_A}\right)^2$ and $cB = \sum_{m_B}\left(C^I_{m_B}\right)^2$, respectively. A last

threshold, t_D, is employed: if $cA > t_D$, state I is localized in unit A; if $cB > t_D$, it is localized in unit B. In all other cases, state I is classified as delocalized. The values of the thresholds t_R, t_{CT}, t_L, and t_D are discussed below.

The method for spectrum decomposition proposed above is certainly not unique, and other criteria and threshold values could be invoked. Besides that, it depends on the approximate validity of a few hypotheses. First, we assume the adequacy of CIS wavefunctions to describe the electronic density. Second, we also assume that the usage of time-dependent DFT amplitudes together with Kohn–Sham orbitals results in an acceptable representation of the CIS wavefunction. Third, we assume that the density partition among the units is uniquely defined, even though the molecular orbitals (Kohn–Sham or Hartree–Fock) are not unique and the Mulliken partition employed is somewhat arbitrary. Due to all these factors, we should take the decomposition as a qualitative analysis of the several contributions to each band, rather than an exact numerical analysis.

4 Computational details

Minimum-energy geometries of ground and excited states were optimized at density functional theory (DFT) and time-dependent functional theory (TDDFT) [27] levels. The long-range corrected CAM-B3LYP functional [28] was employed for most of calculations, since it provides a good description of both localized and delocalized excitations [29]. The aug-cc-pVDZ, aug-cc-pVTZ [30], def2-TZVPP [31], and the TZVP + mod basis sets were used. The latter is the standard def2-TZVP basis set [31] with an extra set of diffuse s and p functions on the heavy atoms. The exponents of these extra Gaussian functions were obtained as 1/3 of the most diffuse exponent of each kind. Complementary calculations were performed with the resolution-of-identity coupled-cluster to the second-order method (RI-CC2) [32–34]. Cartesian coordinates are given in the Online Resource 1.

Time-dependent functional theory electronic structure calculations were performed with Gaussian 09 [35]. RI-CC2 calculations were performed with Turbomole [36]. Spectra were simulated with the Newton-X program [37, 38] interfaced to Gaussian 09.

5 Vertical spectra

5.1 Vertical excitation of furan

Due to several reasons, including its small size, complex spectrum mixing valence and Rydberg states, relation to other pentacyclic molecules, and availability of gas-phase experimental data, furan has been adopted as a benchmark molecule for most of quantum-chemical methods. Good comparative investigations involving diverse theoretical methods are reported in Refs. [39, 40].

In Table 1, we report results for the vertical spectrum of furan at TDDFT and RI-CC2. The multireference general-model-space coupled-cluster (GMS CCSD) results from Ref. [40] are given as well. The low-energy region of furan vertical spectrum is dominated by the $^1B_2$ $\pi\pi^*$ transition, whose experimental maximum is at 6.04 eV [41]. In Sect. 6.1, we will see that the vertical excitation is placed by 0.15 eV higher than the band maximum. Applying this same shift to the experimental result implies that the "experimental vertical excitation" should lie at 6.19 eV. The TD-CAM-B3LYP results, red-shifted by only 0.06 eV in relation to this estimate, are in very good agreement with the experimental result. Both coupled-cluster results are blue-shifted by more than 0.2 eV. This shift is due to the intrinsic difficulty of Hartree–Fock-based methods (multireference or not) to describe the ionic V state [42].

5.2 Vertical excitation of benzene

The vertical spectrum of benzene is reported in Table 2. Additionally to TDDFT and RI-CC2 results computed in this work, the results of the symmetry adapted cluster configuration interaction (SAC-CI) method from Ref. [43] are reported for comparison as well.

The first state is a dark $^1B_{2u}$ $\pi\pi^*$ transition. Its experimental value is 4.9 eV [44] at the band maximum. We discuss later (Sect. 6.2) that the "experimental vertical excitation" is at 5.07 eV. TD-CAM-B3LYP substantially overestimates this transition, which lies at 5.50 eV for both basis sets investigated. RI-CC2 result (5.25 eV) and, especially, SAC-CI (5.06 eV) are in much better agreement with the experiment. The next state, also dark, is a $^1B_{1u}$ $\pi\pi^*$ transition. The "experimental vertical excitation" is at 6.53 eV in this case. RI-CC2 has the smallest deviation to this value. SAC-CI and TD-CAM-B3LYP underestimate the energy of this transition by more than 0.3 eV. The experimental bright $\pi\pi^*$ transition ($^1E_{1u}$) is centered at 6.94 eV, with vertical excitation at 7.07 eV. TD-CAM-B3LYP and RI-CC2 results are in very good agreement with this value. SAC-CI result is blue-shifted by 0.4 eV. All three Rydberg states for which experimental information is available in Table 2 are well described by all methods.

5.3 Vertical excitation and emission of 2-phenylfuran

The ground-state geometry of 2-phenylfuran was optimized at B3LYP/TZVPP and CC2/TZVPP levels. Geometries

Table 1 Vertical excitations of furan with different methods

	TD-CAM-B3LYP				RI-CC2		GMS CCSD[a]	Expt.[b]	Assignment
	aug-cc-pVTZ		TZVP + mod		aug-cc-pVTZ				
	ΔE (eV)	f	ΔE (eV)	f	ΔE (eV)	f	ΔE (eV)	ΔE (eV)	
A_2	5.93	0.000	6.02	0.000	6.02	0.000	5.94	5.91	π–Ryd(s)
B_2	**6.13**	**0.167**	**6.13**	**0.164**	**6.41**	**0.186**	**6.51**	**6.04 (6.19)**[c]	**π–π^***
B_1	**6.44**	**0.037**	**6.56**	**0.041**	**6.55**	**0.038**	**6.46**	**6.47**	**π–Ryd(p_{yz})**
A_2	6.63	0.000	6.81	0.000	6.71	0.000	6.61	6.61	π–Ryd(p_{yz})
A_1	6.97	0.000	6.97	0.000	6.75	0.000	6.89		π–π^*
B_1	7.12	0.001	7.32	0.002	7.23	0.003	7.14		π–Ryd(d_{yz})
A_2	7.10	0.000	7.09	0.000	7.20	0.000	7.00		π–Ryd (p_{yz})
B_2	7.11	0.008	7.07	0.005	7.21	0.004	6.87	6.75	π–π^*

TDDFT results with the B3LYP/TVPP ground-state geometry. RICC2 results with CC2/TZVPP ground-state geometry. Bright states are shown in bold face

[a] Ref. [40]

[b] Data reported in Ref. [39]

[c] "Experimental vertical excitation." See text

Table 2 Vertical excitations of benzene with different methods

	TD-CAM-B3LYP				RI-CC2		SAC-CI[a]	Expt.[b]	Assignment
	TZVP + mod		aug-cc-pVTZ		aug-cc-pVTZ				
	ΔE (eV)	f	ΔE (eV)	f	ΔE (eV)	f	ΔE (eV)	ΔE (eV)	
B_{2u}	5.50	0.000	5.50	0.000	5.25	0.000	5.06	4.90 (5.07)[c]	π–π^*
B_{1u}	6.16	0.000	6.16	0.000	6.47	0.000	6.22	6.20 (6.53)	π–π^*
E_{1g}	6.55	0.000	6.45	0.000	6.47	0.000	6.42	6.33	π–Ryd(s)
A_{2u}	**7.03**	**0.068**	**6.95**	**0.068**	**7.00**	**0.064**	**7.06**	**6.93**	**π–Ryd(p_{yz})**
E_{1u}	**7.05**	**0.607**	**7.05**	**0.614**	**7.15**	**0.665**	**7.48**	**6.94 (7.07)**	**π–π^***
E_{2u}	7.14	0.000	7.05	0.000	7.06	0.000	7.12	6.95	π–Ryd(p_{yz})
A_{1u}	7.28	0.000	7.17	0.000	7.14	0.000	7.19	–	π–Ryd(p_{yz})

TDDFT results with the B3LYP/TVPP ground-state geometry. RICC2 results with CC2/TZVPP ground-state geometry. Bright states are shown in bold face

[a] Ref. [43]

[b] Band maxima as surveyed in Ref. [43]

[c] The values in parenthesis are the "experimental vertical excitations." See text

calculated at both levels are similar. In particular, the phenyl and furans rings are twisted with a dihedral angle around 14° for both levels of theory.

The bright states of the vertical excitation spectrum of 2-phenylfuran in gas phase are reported in Table 3. The full set of vertical transitions up to 7.4 eV is reported in Table S1 of the Online Resource 1. The first two transitions are into a bright and a dark excimer states at 4.66 and 4.98 eV, respectively. The experimental band maximum in this region is at 4.55 eV in hexanes [16] and at 4.44 eV in methanol [45]. After a series of dark transitions into Rydberg states, a second band is characterized by a local $\pi\pi^*$ excitation within the benzene ring (5.98 eV) and a $\pi\pi^*$ excitation delocalized over the whole molecule. A very bright benzene-localized transition appears high in the spectrum at 7.02 eV. A less intense transition at 7.38 eV marks the fourth band.

The dependence of the vertical spectrum on the theoretical method can be accessed with the data of Table 3. TD-CAM-B3LYP energy of the bright states computed with aug-cc-pVDZ and aug-cc-pVTZ basis sets differs by less than 0.03 eV, with systemically lower values when using the triple-ζ basis set. RI-CC2 and TD-CAM-B3LYP predict very consistent results for the spectrum as well. The largest difference is observed in the lowest state, for which CC2 result is 0.19 eV higher than that at TDDFT level. For the other states, the energy difference is always smaller than 0.08 eV.

Table 3 Bright vertical excitations and emission of 2-phenylfuran with different methods

Assignment	TD-CAM-B3LYP				RI-CC2		Expt.
	aug-cc-pVDZ		aug-cc-pVTZ				
	ΔE (eV)	f	ΔE (eV)	f	ΔE (eV)	f	ΔE (eV)
Absorption							
π(PF)–π^*(PF)	4.66	0.530	4.65	0.529	4.84	0.546	4.44[a] (4.54)[c] 4.55[b] (4.64)[c]
π(P)–π^*(P)	5.98	0.092	5.96	0.089	5.96	0.085	
π(PF)–π^*(PF)	6.19	0.107	6.16	0.116	6.08	0.080	
π(P)–π^*(P)	7.02	0.399	6.99	0.335	7.07	0.387	
Emission							
π(PF)–π^*(PF)	3.94	−0.562	3.99	−0.559	4.28	−0.575	3.97[b]

TDDFT using B3LYP/TZVPP ground-state geometry. RI-CC2 absorption: aug-cc-pVTZ with CC2/TZVPP ground-state geometry. Emission: S_1-minimum geometry optimized at the same level as the reported single point

[a] Band maximum in methanol. Ref. [45]

[b] Band maximum in hexanes. Ref. [16]

[c] "Experimental vertical excitation." See text

The geometry of the S_1 state of 2-phenylfuran was optimized at RI-CC2/TZVPP, TD-CAM-B3LYP/aug-cc-pVDZ and TD-CAMB3LYP/aug-cc-pVTZ levels of theory. The emission energy is given in Table 3 for these levels. TDDFT geometries are planar, while the CC2 geometry holds a small degree of puckering at the bridge carbon atom of the phenyl ring (CCCO dihedral = 11°). The CC bridge is shorten from 1.45 Å in the ground state to 1.40 Å in the excited state.

For all cases, the S_1 state corresponds to a delocalized $\pi\pi^*$ transition with large absolute value of oscillator strength. With the triple-ζ basis set, TDDFT vertical emission energy is 3.99 eV, which is 0.05 eV higher than the double-ζ result. Both results are in good agreement with the band maximum, located at 3.97 eV [16]. The RI-CC2 result, 4.28 eV, is blue-shifted in comparison to the experiment.

6 Spectrum simulations

6.1 Absorption spectrum of furan

Furan absorption cross section is shown in Fig. 2. Absorption was computed with Eq. (23), and the parameters employed in the simulations are given in Table 4. Vibronic shifts were set to zero, and all lines were assumed to have the same width δ_n. Eight excited states for each one of the 350 ensemble points were computed. The gray area indicates the error in the numerical integration computed with Eq. (25).

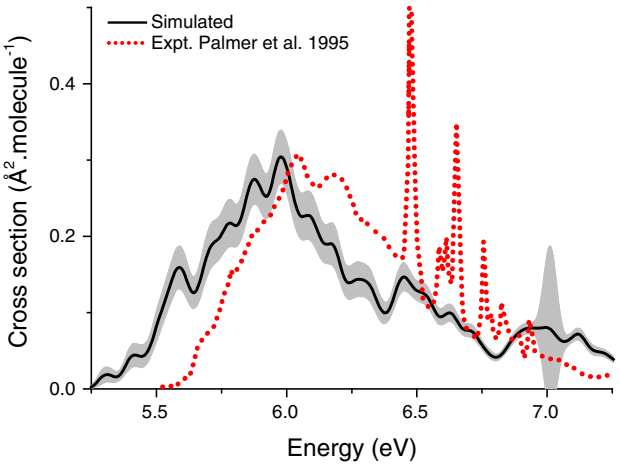

Fig. 2 Simulated (TD-CAM-B3LYP/TZVP-mod) and experimental absorption cross section of furan in gas phase. Experimental data from Ref. [41]

The experimental data, also in gas phase, is from Ref. [41]. In the region below 7 eV, furan shows a series of Rydberg states over-imposed to a broad band. The nuclear-ensemble method provides a good qualitative prediction of the spectrum. The intensity and the shape of the broad band are in very good agreement with the experiment. The energy shift is caused by the electronic structure method (see Sect. 5.1), rather than by the spectrum simulation method itself.

The broad band is due to the bright $\pi\pi^*$ state. The maximum of this band in the simulated spectrum is at 5.98 eV, slightly red-shifted in comparison with the experimental result, 6.04 eV [41]. The corresponding vertical excitation is the 1^1B_2 transition (see Table 1), which

Table 4 Parameters employed for spectrum simulations in this work

		δ_n (eV)	N_p	N_{fs}	n_r
Absorption					
Furan	Fig. 2	0.05	350	8	1
Benzene	Fig. 3-left	0.02	10,000	1	1
Benzene	Fig. 3-center	0.02	10,000	4	1
Benzene	Fig. 3-right	0.05	500	10	1
2-Phenylfuran	Fig. 4-top	0.05	850	23	1.375
2-Phenylfuran	Fig. 4-bottom	0.05	850	23	1.375
Emission ($T = 0$ K)					
2-Phenylfuran	Fig. 5	0.05	850	1	1

Absorption: Eq. (23) with Gaussian line shapes and $\varepsilon_n = 0.0$ eV. Emission: Eq. (34) with Lorentzian line shapes

lies at 6.13 eV, therefore, 0.15 eV higher than the band maximum. The sum of this shift to the experimental band maximum defines the "experimental vertical excitation" shown in Table 1.

The two main limitations of the current implementation of the nuclear-ensemble approach are clear in the simulations for furan: First, the lack of vibrational resolution: while the experimental results show a vibrational structure near the maximum, the simulations predict only the envelope of the band (the apparent oscillations are numerical noise). Second, the wrong band width for long-lived states: long-lived states give rise to very thin peaks in the spectrum, which are not correctly described in the simulations. Both limitations are caused by the overlap-function approximation (Eq. 15), which neglects the excited-state wave packet evolution (see discussion in Sect. 2.6).

6.2 Absorption spectrum of benzene

The simulated and experimental results for the three bands below 7 eV are shown in Fig. 3. The simulated absorption spectrum was computed with Eq. (23) with numerical-integration error (gray area) given by Eq. (25). Parameters are given in Table 4. The vibronic shift ε_n was assumed to be zero. An estimate for this shift is discussed below. Specific line widths were not computed, and all lines were assumed to have the same width δ_n given in Table 4. The number of excited states (up to 10) and the number of points in the ensemble (up to 10,000) were set differently for each region of the spectrum.

In the region below 7 eV, benzene absorbs in three distinct bands. The first is a dark band around 5 eV; the second is low-intensity band around 6.2 eV; and the third is a bright band around 7 eV. Very high-resolution measurements of the dark band along with a good review of previous spectroscopic data for benzene can be found in Ref. [46]. The UV absorption spectra of benzene vapor over a large wavelength domain are available in Refs. [44, 47, 48]. For comparison with the present simulations, we have taken the results from Ref. [44].

There is an overall good qualitative agreement between the simulations and the experimental results (Fig. 3). Absolute intensities are very well reproduced, especially if we take into account that they span three orders of magnitude over the three bands. Once more, vibrational resolution and long-lived states (narrow peaks) are not described. Besides that, the main deviations between theory and experiment are the energy shifts observed in the dark and in the intermediary bands. These shifts, however, are not caused by the spectrum simulation itself, but they are caused by the uncertainties of the electronic structure method and level, in this case, the TD-CAM-B3LYP/TZVP-mod, as we have discussed in Sect. 5.2.

Other source of band shift is vibronic corrections, but they are much smaller than the shift caused by the electronic structure method. In the case of the first energy band of benzene (Fig. 3-left), we can employ Eq. (20) to estimate the vibronic shift. At TD-CAM-B3LYP/TZVP-mod level, $\Delta E_{0,1} = 5.548$ eV and $\Delta E^a_{0,1} = 5.421$ eV, and therefore $\varepsilon_1 = -0.06$ eV, which is much smaller than the shift observed between theory and experiment in Fig. 3-left, about -0.6 eV from maximum to maximum.

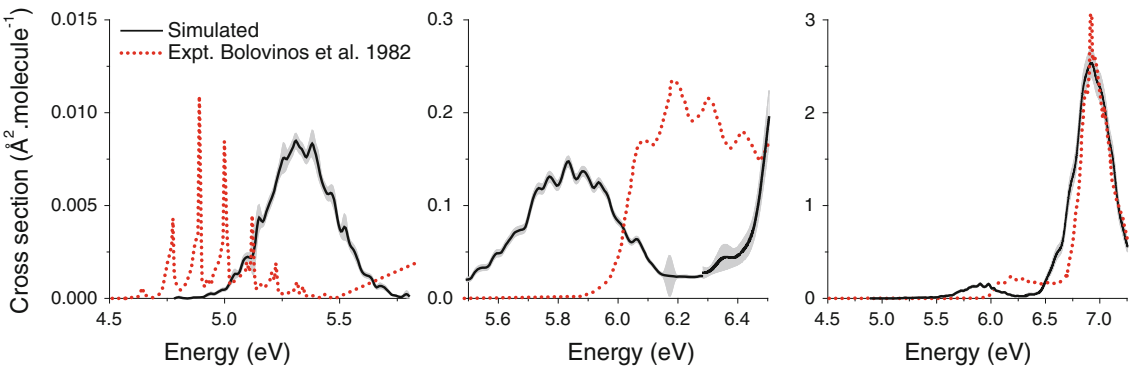

Fig. 3 Simulated (TD-CAM-B3LYP/TZVP-mod) and experimental absorption cross section of benzene vapor. Experimental data from Ref. [44]

For each of the three bands, the comparison between the simulated band maximum and the corresponding vertical excitation is 0.17 eV for the first band (B_{2u}), 0.33 eV for the second band (B_{1u}), and 0.13 eV for the third band (E_{1u}). These deviations were summed to the experimental band centers to give the "experimental vertical excitations" shown in Table 2.

6.3 Absorption spectrum of 2-phenylfuran

The absorption cross section of 2-phenylfuran is shown in Fig. 4. As for the previous cases, the simulated absorption was computed with Eq. (23) with numerical-integration error (gray area) given by Eq. (25). Parameters are given in Table 4. Vibronic shifts were set to zero, and all lines were assumed to have the same width δ_n. To cover the excitation-energy domain under 7 eV, 23 excited states were computed for each one of the 850 ensemble points. Note that the number of points in the ensembles for furan (350), benzene (500) and 2-phenylfuran (850) was chosen to be proportional to the number of degrees of freedom of each one of these molecules. The number of excited states was chose in each case as the minimum necessary do describe the spectrum up to 7 eV.

Experimental data for absorption of 2-phenylfuran were reported in Ref. [16] in hexanes (also shown in Fig. 4-top) and in Ref. [45] in methanol. Different from benzene and furan, 2-phenylfuran absorbs with appreciable intensity below 5 eV, with a band centered at 4.56 eV (expt.: 4.55 eV [16]). The simulations predict other two band of similar intensity at 6.00 eV and 6.86 eV, and a less intense band at 7.29 eV. The experimental result also indicates the raise of a second band around 6 eV, but the information is limited in this region. Overall, the simulated spectrum is in good agreement with the experiment. Intensities are very well reproduced, and the band shift is much smaller than in the simulations of furan and benzene, probably by error compensation due to the comparison between gas-phase simulations and solvated experiments.

Another noticeable difference between the spectrum of 2-phenylfuran and that of the isolated monomers is the intensity around 7 eV. While the absorption cross section of benzene is very high in this region (2.5 $Å^2$ $molecule^{-1}$), the absorption cross section of 2-phenylfuran is only about 1/3 of this value. This reduction in the absorption intensity is a direct effect of the delocalization of the orbitals over the whole molecule, reducing the transition moments.

Figure 4—bottom—shows the decomposition of the spectrum of 2-phenylfuran in terms of the several classes of states. The spectrum-decomposition method explained in Sect. 3 was applied for each of the $N_p \times N_{fs} = 19{,}550$ lines composing the spectrum. The threshold values are $t_R = 0.9$, $t_{CT} = 0.6$, $t_L = 0.8$, and $t_D = 0.35$. These values

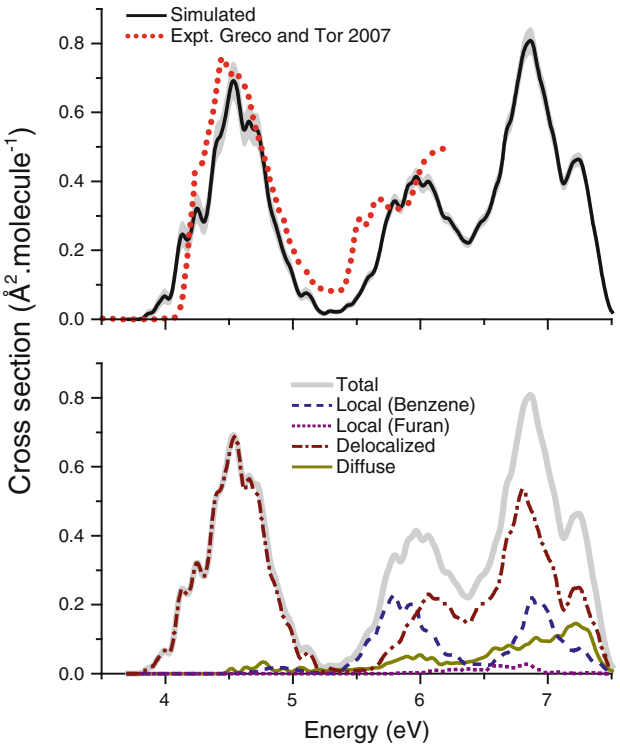

Fig. 4 *Top* simulated (TD-CAM-B3LYP/aug-cc-pVDZ) and experimental absorption cross section of 2-phenylfuran. Experimental data in hexanes from Ref. [16]. *Bottom* Spectrum decomposition. CT contributions are negligible and are not shown

were chosen after making a visual assignment of the states at the ground-state geometry. Having the decomposition, the spectrum for each class was recomputed with Eq. (23) including only the transitions belonging to the respective class, but still keeping the total N_p value.

As expected, the lowest-energy band (4.56 eV) is due to delocalized excitations involving both phenyl and furan rings. Delocalized excitations are also the major contributions for the other two bands. In the case of the band at 6.00 eV, localized excitations within benzene ring are as important as the delocalized states. In the third band (6.86 eV), benzene-localized states and diffuse states give minor contributions to the band. The fourth band (7.29 eV) is mainly due to delocalized excitations with large contributions of diffuse states. For the whole spectrum, local excitations within the furan ring are negligible, while charge-transfer states do not register in the scale of this graph.

It is instructive to compare the vertical excitations provided in Table 3 and the bands show in Fig. 4. The bright vertical excitation in the lowest band (S_1: 4.66 eV) is 0.1 eV higher than the band maximum. This shift is summed to the experimental band maximum to provide the "experimental vertical excitations" in Table 3 and in Table S1 of the Online Resource 1. The delocalized $\pi\pi^*$ character of this vertical excitations is the same as the character

of the whole band. The second band, whose corresponding vertical excitations are S_6 and S_7, is centered exactly in between the energies of these two states. While S_6 is a benzene-localized state, S_7 is a delocalized state, which corresponds to the two sub-bands revealed by the spectrum decomposition shown in Fig. 4-bottom. The third band at 6.86 eV is related to the vertical excitation at 7.02. The assignment in this case is not straightforward as for the other two bands. The vertical excitation S_{17} is a benzene-localized $\pi\pi^*$ excitation. The spectrum decomposition, however, shows that the major contribution to this band comes from delocalized excitations, with secondary contributions from benzene-localized excitations. This difference occurs because the degree of localization depends on the nuclear geometry, and for this specific state, this quantity is very near the adopted threshold. For most of points in the nuclear-ensemble, the degree of localization was below the threshold $t_D = 0.35$. Specifically for the ground state minimum, this quantity was 0.36 (see *cA* in Table S2 of the Online Resource 1), just enough to make the transition to be classified as localized.

6.4 Emission spectrum of 2-phenylfuran

The simulated differential emission rate for 2-phenylfuran computed with Eq. (34) is shown in Fig. 5, together with experimental data from Ref. [16]. The simulated emission was computed with Eq. (34). The numerical-integration error (gray area) was computed with an expression similar to Eq. (25), but for the differential emission rate. Parameters are given in Table 4. All lines were assumed to have the same width δ_n. An ensemble of 850 points was built around the minimum of the S_1 state assuming $T = 0$ K.

Because the experimental data are given in arbitrary units, in Fig. 5, it has been normalized to match the maximum intensity of the simulated spectrum. The fluorescence of 2-phenylfuran shows a single band. The maximum of the simulated data occurs at 3.85 eV, while for the experimental data, it is at 3.97 eV. In spite of the good agreement between the theoretical and experimental results, one can observe that the asymmetry of the experimental band is not fully reproduced in the simulations.

Using Eq. (36), the maximum radiative lifetime is $\tau_0 = 3.1 \pm 0.2$ ns. With the normalization adopted in Fig. 5, the experimental value is $\tau_0 = 3.2$ ns. This same quantity is usually estimated based on the values of the energy gap and oscillator strength obtained at the excited-state minimum geometry ($\mathbf{R}_{S_1\,\mathrm{min}}$), where it is given by

$$\frac{1}{\tau_0} = \frac{e^2 n_r^3}{2\pi\hbar^2 mc^3\varepsilon_0}\Delta E_{1,0}(\mathbf{R}_{S_1\,\mathrm{min}})^2 |f_{01}(\mathbf{R}_{S_1\,\mathrm{min}})|. \quad (43)$$

Employing this last equation, which assumes the validity of the Condon approximation, the lifetime is 2.6 ns ($n_r = 1$), somewhat shorter than the value obtained from the simulated spectrum.

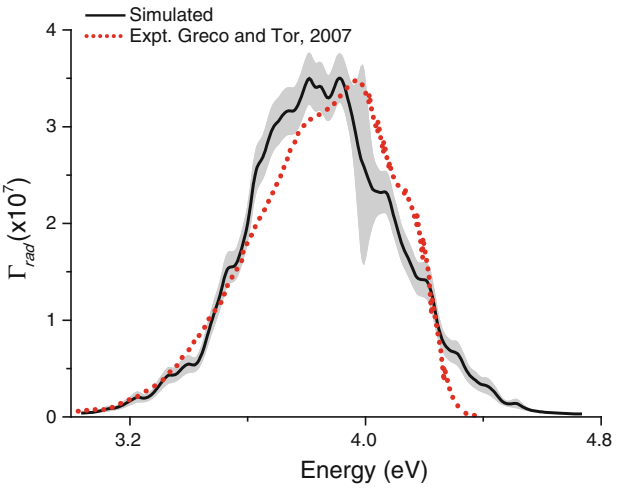

Fig. 5 Simulated (TD-CAM-B3LYP/aug-cc-pVDZ) and experimental emission spectrum of 2-phenylfuran. Experimental data of Ref. [16] normalized by the maximum of the simulated data

7 Conclusions

Simulations of electronic spectra based on nuclear-ensemble are an efficient approach for theoretical investigations of large molecules, especially when post-Condon features play a major role. The formal derivation of the method presented in this work enhances the approximations employed in the method and allows proposing new developments that will be explored in further works.

The nuclear-ensemble approach is especially well tailored to investigate how different properties contribute to each band in the spectrum. In particular, we have proposed and implemented a method for spectrum decomposition in terms of the contributions from different classes of states (localized, delocalized, diffuse and charge-transfer).

Using the nuclear-ensemble approach, we have simulated the absorption spectra of benzene, furan and 2-phenylfuran in gas phase. Based on these simulations, "experimental vertical excitations" were estimated. For the three molecules, the main bands were assigned and the spectrum-decomposition method was applied to 2-phenylfuran.

The absorption spectrum of 2-phenylfuran is composed of four bands between 4.5 and 7.5 eV. The lowest band is almost purely due to excimer states. The other bands are still dominated by delocalized states, but with relevant contributions from benzene-localized states and diffuse states. Furan-localized and charge-transfer states play a minor role in the absorption of 2-phenylfuran.

The emission spectrum of 2-phenylfuran is characterized by a single band centered at 3.9 eV and with a radiative lifetime of 3.2 ns. This value, which is obtained by integration of the full emission spectrum, is larger than the 2.6 ns predicted by a usual Condon approximation.

Spectrum simulations were based on TDDFT with the CAM-B3LYP functional. Methodological comparisons with RI-CC2 and other methods showed that TD-CAM-B3LYP have a very good performance for furan, 2-phenylfuran and the bright band of benzene. Substantial energy shifts, however, were observed for the dark bands of benzene.

Acknowledgments The authors acknowledge the fruitful discussions with Dr. Jan Goetze. This work is a contribution to the Festschrift issue in honor of Prof. Chaer Nascimento, who was co-advisor of the doctoral work of one of the authors (MB). Nascimento's insightful analysis of fundamental issues in quantum chemistry [49] has inspired a whole generation of computational theoretical chemists.

References

1. Koppel H, Domcke W, Cederbaum LS (1984) Adv Chem Phys 57:59
2. Niu Y, Peng Q, Deng C, Gao X, Shuai Z (2010) J Phys Chem A 114:7817
3. Tannor DJ, Heller EJ (1982) J Chem Phys 77:202
4. Petrenko T, Neese F (2007) J Chem Phys 127:164319
5. Barone V, Bloino J, Biczysko M, Santoro F (2009) J Chem Theory Comput 5:540
6. Improta R, Barone V, Santoro F (2007) Angew Chem 119:409
7. Barbatti M, Aquino AJA, Lischka H (2010) Phys Chem Chem Phys 12:4959
8. Svoboda O, Oncak M, Slavícek P (2011) J Chem Phys 135:154301
9. Bergsma JP, Berens PH, Wilson KR, Fredkin DR, Heller EJ (1984) J Phys Chem 88:612
10. Saven JG, Skinner JL (1993) J Chem Phys 99:4391
11. Kubo R (1969) Adv Chem Phys 15:101
12. Schinke R (1995) Photodissociation dynamics: spectroscopy and fragmentation of small polyatomic molecules. Cambridge University Press, Cambridge
13. Crespo-Otero R, Barbatti M (2011) J Chem Phys 134:164305
14. Barbatti M (2011) Phys Chem Chem Phys 13:4686
15. Szalay PG, Aquino AJA, Barbatti M, Lischka H (2011) Chem Phys 380:9
16. Greco NJ, Tor Y (2007) Tetrahedron 63:3515
17. Sakurai JJ (1994) Modern quantum mechanics. Addison-Wesley, Massachusetts
18. Hilborn RC (1982) Am J Phys 50:982
19. Lepage GP (1978) J Comput Phys 27:192
20. Lukes V, Solc R, Barbatti M, Lischka H, Kauffmann HF (2010) J Theor Comput Chem 9:249
21. Rikken GLJA (1995) Physica B 204:353
22. Lampert RA, Meech SR, Metcalfe J, Phillips D, Schaap AP (1983) Chem Phys Lett 94:137
23. Feynman RP (1982) Statistical mechanics: a set of lectures. The Benjamin/Cummings Publishing Company, London
24. Heller EJ (1981) Acc Chem Res 14:368
25. Worth GA, Cederbaum LS (2004) Annu Rev Phys Chem 55:127
26. Meister J, Schwarz WHE (1994) J Phys Chem 98:8245
27. Casida M (1995) Time-dependent density functional response theory for molecules. In: Chong D (ed) Recent advances in density functional methods, part I. World Scientific, Singapore, p 155
28. Yanai T, Tew DP, Handy NC (2004) Chem Phys Lett 393:51
29. Peach MJG, Benfield P, Helgaker T, Tozer DJ (2008) J Chem Phys 128:044118
30. Dunning TH (1989) J Chem Phys 90:1007
31. Weigend F, Häser M, Patzelt H, Ahlrichs R (1998) Chem Phys Lett 294:143
32. Christiansen O, Koch H, Jorgensen P (1995) Chem Phys Lett 243:409
33. Hättig C, Weigend F (2000) J Chem Phys 113:5154
34. Hättig C, Köhn A (2002) J Chem Phys 117:6939
35. Frisch MJ, Trucks GW, Schlegel HB, Scuseria GE, Robb MA, Cheeseman JR, Scalmani G, Barone V, Mennucci B, Petersson GA, Nakatsuji H, Caricato M, Li X, Hratchian HP, Izmaylov AF, Bloino J, Zheng G, Sonnenberg JL, Hada M, Ehara M, Toyota K, Fukuda R, Hasegawa J, Ishida M, Nakajima T, Honda Y, Kitao O, Nakai H, Vreven T, Montgomery J, J. A., Peralta JE, Ogliaro F, Bearpark M, Heyd JJ, Brothers E, Kudin KN, Staroverov VN, Kobayashi R, Normand J, Raghavachari K, Rendell A, Burant JC, Iyengar SS, Tomasi J, Cossi M, Rega N, Millam NJ, Klene M, Knox JE, Cross JB, Bakken V, Adamo C, Jaramillo J, Gomperts R, Stratmann RE, Yazyev O, Austin AJ, Cammi R, Pomelli C, Ochterski JW, Martin RL, Morokuma K, Zakrzewski VG, Voth GA, Salvador P, Dannenberg JJ, Dapprich S, Daniels AD, Farkas Ö, Foresman JB, Ortiz JV, Cioslowski J, Fox DJ (2009). Gaussian 09, revision A02. Gaussian, Inc., Wallingford
36. Ahlrichs R, Bar M, Haser M, Horn H, Kolmel C (1989) Chem Phys Lett 162:165
37. Barbatti M, Granucci G, Ruckenbauer M, Plasser F, Pittner J, Persico M, Lischka H (2011). NEWTON-X: a package for Newtonian dynamics close to the crossing seam. www.newtonx.org
38. Barbatti M, Granucci G, Persico M, Ruckenbauer M, Vazdar M, Eckert-Maksic M, Lischka H (2007) J Photochem Photobiol A 190:228
39. Wan J, Meller J, Hada M, Ehara M, Nakatsuji H (2000) J Chem Phys 113:7853
40. Li X, Paldus J (2010) J Phys Chem A 114:8591
41. Palmer MH, Walker IC, Ballard CC, Guest MF (1995) Chem Phys 192:111
42. Angeli C (2009) J Comput Chem 30:1319
43. Li Y, Wan J, Xu X (2007) J Comput Chem 28:1658
44. Bolovinos A, Philis J, Pantos E, Tsekeris P, Andritsopoulos G (1982) J Mol Spectrosc 94:55
45. Abu-Eittah R, Hilal R, Hamed MM (1981) Int J Quantum Chem 19:383
46. Fally S, Carleer M, Vandaele AC (2009) J Quant Spectrosc Radiat Transf 110:766
47. Pantos E, Philis J, Bolovinos A (1978) J Mol Spectrosc 72:36
48. Suto M, Wang X, Shan J, Lee LC (1992) J Quant Spectrosc Radiat Transf 48:79
49. Nascimento M, Barbosa A (2003) Quantum mechanics of many-electrons systems and the theories of chemical bond. In: Brändas EJ, Kryachko E (eds) Fundamental world of quantum chemistry, vol 1. Kluwer, Dordrecht, p 371